

Quasi-periodic Eruptions from Stellar-mass Black Holes Impacting Accretion Disks in Galactic Nuclei

KUN LIU (刘坤) ¹, SHANG-FEI LIU (刘尚飞) ^{1,2}, ZHEN PAN (潘震) ^{3,4}, HONGPING DENG (邓洪平) ⁵,
RONGFENG SHEN (申荣锋) ^{1,2} AND CONG YU (余聪) ^{1,2}

¹*School of Physics and Astronomy, Sun Yat-sen University, Zhuhai 519082, China*

²*CSST Science Center for the Guangdong-HongKong-Macau Great Bay Area, Sun Yat-sen University, Zhuhai 519082, China*

³*Tsung-Dao Lee Institute, Shanghai Jiao-Tong University, 520 Shengrong Road, Shanghai 201210, China*

⁴*School of Physics & Astronomy, Shanghai Jiao-Tong University, 800 Dongchuan Road, Shanghai 200240, China*

⁵*Shanghai Astronomical Observatory, Chinese Academy of Sciences, 80 Nandan Road, Shanghai 200030, China*

ABSTRACT

We investigate the origins of quasi-periodic eruptions (QPEs) in galactic nuclei using global three-dimensional meshless finite-mass (MFM) simulations. By modeling stellar and black-hole impactors traversing accretion disks under various inclinations and surface densities, we evaluate their consistency with the observed properties of QPEs. Stellar impacts produce highly asymmetric bipolar ejecta with forward outbursts dominating by over an order of magnitude in energy and luminosity due to the star blocking downstream flow and creating a low-density wake. This shock-compression mechanism often renders backward events unobservable, implying one detectable burst per orbit, and challenging the standard assumption of two bursts. It also fails to explain alternating long-short recurrence patterns and places several sources near or within twice the tidal disruption radius for solar-mass stars, raising severe stability concerns. Whereas a stellar-mass black hole (sBH) gravitationally focuses and heats disk gas extending from its Bondi radius R_B to its Hill radius R_H during an impact, yielding nearly symmetric ejecta with mild contrasts. This gravitational-drag mechanism generates higher energy budgets at low inclinations due to enhanced mass accumulation. We suggest an ad hoc effective interaction radius $R_{\text{eff}} \simeq 0.5 R_B^{1/3} R_H^{2/3}$ to quantify this trend. Our semi-analytical model confirms that sBH-disk collisions can power the full QPE energy range ($10^{44} - 10^{48}$ erg), naturally accounting for periodicity, asymmetry, durations and diversity.

Keywords: High Energy astrophysics (739) — X-ray transient sources (1852) — Black holes (162) — Active galactic nuclei (16) — Hydrodynamics (1963) — Tidal disruption (1696)

1. INTRODUCTION

Quasi-periodic eruptions (QPEs) represent a puzzling new class of soft X-ray transients discovered in the past decade, characterized by recurring flares superimposed on a quiescent continuum of active galactic nuclei (AGNs). QPEs feature bursts lasting several thousand seconds, with recurrence intervals from hours to days and flux increases of ~ 10 – 100 times in the soft X-ray band (0.1–0.2 keV) (M. Giustini et al. 2020; A. Chashkina et al. 2024). The first QPEs were discovered by the XMM-Newton satellite in GSN 069 (G. Miniutti et al. 2019) and RX J1301.9+2747 (L. Sun et al. 2013; M. Giustini et al. 2020), followed by eROSITA detections of eRO-QPE1-5 (R. Arcodia et al. 2021, 2024, 2025).

Recent additions include Ansky, AT2022upj and J2344 in 2025 and 2026 (L. Hernández-García et al. 2025a; J. Chakraborty et al. 2025; P. Baldini et al. 2026), highlighting their diversity and potential prevalence in time-domain surveys.

QPEs often link to tidal disruption events (TDEs); for instance, they appear $\mathcal{O}(1)$ year post-ignition in AT2019qiz (M. Nicholl et al. 2024), XMMSL J0249 (J. Chakraborty et al. 2021) and among several hosts with TDE signatures (N. Jiang & Z. Pan 2025). J. Chakraborty et al. (2025) further estimate that $\sim 10\%$ optical TDEs result in QPEs within 5 yr post-disruption. In parallel, a newly activated AGN (L. Hernández-García et al. 2025a) or a featureless TDE (J. Zhu et al. 2025), host the most energetic QPEs, Ansky, detected so far, exhibiting unusually powerful and puzzling period modulations (J. Chakraborty et al. 2026). Recent observations indicate that QPEs show a prefer-

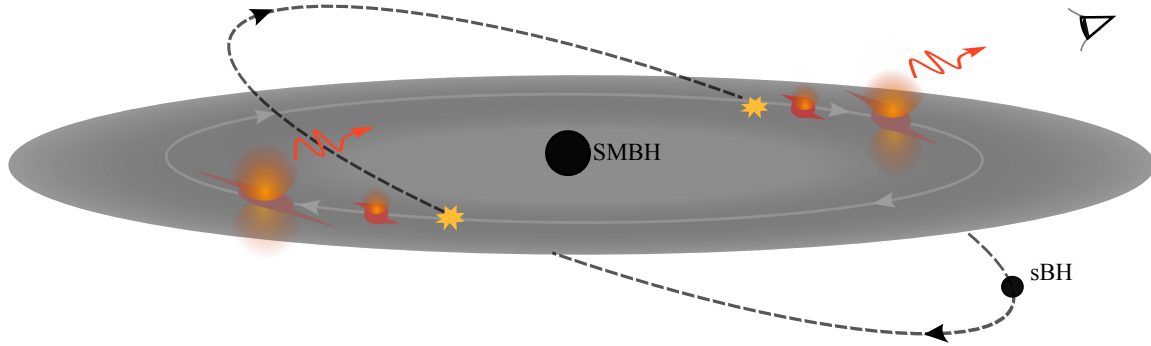


Figure 1. Schematic illustration of an extreme mass-ratio inspirals (EMRIs) system, where a stellar-mass black hole (sBH) moves along a low-inclination orbit and penetrates an optically thick accretion disk with a relative velocity below the local Keplerian speed. During each orbital period, the sBH impacts the disk twice, exciting nearly symmetric ejecta in the vertical directions. The ejecta subsequently expand and cool, evolving into optically thin bubbles through which radiation can escape. Meanwhile, strong gravitational perturbations induce local spiral-shaped density waves in the disk material.

ence for a subset of TDEs in galaxies hosting an extending emission line region (T. Wevers et al. 2022; T. Wevers & K. D. French 2024; Y. Xiong et al. 2025) and/or a parsec scale dust torus (M. Wu et al. 2025).

Unlike the stochastic variability commonly observed in AGN, QPEs commonly exhibit regular patterns, including alternating long – short recurrence times ($T_{\text{long}}, T_{\text{short}}$) or strong – weak amplitudes (G. Miniutti et al. 2019; M. Giustini et al. 2020). C. Zhou et al. (2024a,b) further pointed out that the sum of two consecutive intervals $T_{\text{long}} + T_{\text{short}}$ is often constant, though both T_{long} and T_{short} show clear variations. The eruptions appear as soft X-ray outbursts at 0.1–0.2 keV against a cooler quiescent continuum (0.05–0.08 keV), with flare energies of $10^{40} - 10^{42}$ erg — well below those of tidal disruption events but vastly larger than stellar flares — thereby constraining the underlying energy reservoir. Meanwhile, their hosts typically harbor low-mass supermassive black holes (SMBHs; $M_{\text{BH}} \sim 10^{5-7} M_{\odot}$ (R. Arcodia et al. 2024)), suggesting orbital dynamics in compact regions.

The physical origin of QPEs remains the subject of active debate. A family of models invokes a star on a bound orbit around a supermassive black hole that supplies material to the central engine. In the repeating partial tidal disruption (rpTDE) variant, the star undergoes repeated partial stripping near pericenter, launching short-lived X-ray outbursts (P. A. Evans et al. 2023; D. Pasham et al. 2024). A closely related picture involves steady mass transfer from the orbiting body onto the central black hole, for example through Roche-lobe overflow (RLOF) in stars (I. Zalamea et al. 2010; A. King 2020; Z. Y. Zhao et al. 2022; J. H. Krolik & I. Linial 2022; B. D. Metzger et al. 2022; M. Wang et al. 2022; W. Lu & E. Quataert 2023). Although both pictures can produce periodic flares under favorable conditions, they struggle to sustain stable outbursts over

hundreds of cycles and offer no natural mechanism for the observed alternating long–short recurrence pattern. Moreover, the formation rate of such tight stellar orbits (hours to days) — whether through the loss-cone channel, the Hills mechanism, or Roche-lobe capture — remains orders of magnitude too low to account for the observed QPE population (Z. Pan & D. Lai 2026).

The disk instability model attributes QPE outbursts to intrinsic processes within the accretion disk itself—thermal instabilities, magnetorotational instabilities (MRI), or other spontaneous perturbations (A. Raj & C. J. Nixon 2021; X. Pan et al. 2022, 2023; K. Kaur et al. 2023; M. Śniegowska et al. 2023; H. Deng 2025). With suitable inner-boundary torque and stress prescriptions, this framework can successfully reproduce several observed light-curve and spectral properties of GSN 069 (X. Pan et al. 2022). However, because these instabilities are generated internally, the model lacks a robust external clock capable of enforcing the strict repeating periodicity observed in most QPE sources. Consequently, it struggles to account for the characteristic alternating long–short recurrence intervals and strong–weak amplitude pattern unless additional modulating physics is introduced.

The current most popular explanation invokes an extreme mass ratio inspiral (EMRI) that crosses the accretion disk twice per orbital period, thereby producing two eruptions per orbit (see, eg. Fig. 1; L. J. Dai et al. 2010; J. Xian et al. 2021; P. Suková et al. 2021; A. Franchini et al. 2023; I. Linial & B. D. Metzger 2023; H. Tagawa & Z. Haiman 2023; I. Linial & B. D. Metzger 2024; C. Zhou et al. 2024a,b, 2025; C. Zhou et al. 2025; I. Vurm et al. 2025). The disk itself is naturally supplied by a recent tidal disruption event, which simultaneously accounts for the TDE-QPE association. A mildly eccentric EMRI orbit or differences in the impact angle then naturally gives rise to the alternating long–short recur-

rence intervals and strong–weak flare amplitudes that are characteristic of many sources.

The question of whether the secondary companion is a star or a compact object remains open. [I. Linial & B. D. Metzger \(2023\)](#) argue strongly in favor of a main-sequence star, pointing out that its physical radius ($\sim R_\odot$) is orders of magnitude larger than the Bondi radius of a stellar-mass black hole ($\sim 0.02R_\odot$ for a perpendicular passage of a $100 M_\odot$ black hole). Consequently, a stellar EMRI shocks a much larger column of disk gas per passage, whereas a stellar-mass black hole would simply produce too little shocked material to explain the observed flare luminosities unless the secondary is an intermediate-mass black hole.

Local hydrodynamic simulations that model a stellar EMRI crossing a stationary patch of the accretion disk have been used to test this picture. [P. Z. Yao et al. \(2025\)](#) show that repeated passages drive significant mass loss and expansion of the stellar envelope, limiting the star’s lifetime to at most ~ 1000 yr. The authors therefore propose that the observed QPEs are powered primarily by collisions between the expanding stellar debris stream and the disk, rather than by the intact star itself. [X. Huang et al. \(2025\)](#) performed 2D multi-group radiation-hydrodynamic simulations of a solar-type star colliding with a thin disk and showed that the interaction produces asymmetric bipolar ejecta, with prominent forward breakout emission leading to sharply peaked light curves and large luminosity contrasts between the two sides. The resulting flares reach peak bolometric luminosities $\gtrsim 10^{43}$ erg s $^{-1}$, have durations of sub-hour to a few hours, and exhibit SEDs that peak in the extreme-UV (20–50 eV) with soft X-ray luminosities $\nu L_\nu \gtrsim 10^{42}$ erg s $^{-1}$, broadly consistent with short-period QPEs. However, both studies highlight persistent challenges: strong ejecta asymmetry, relatively short flare durations, and the difficulty of sustaining long-term stable outbursts.

However, local approximations ([P. Z. Yao et al. 2025](#); [X. Huang et al. 2025](#)) that neglect the central SMBH’s gravity effectively treat the secondary’s Hill radius as infinite, i.e. all the gas in the simulation domain will be affected. In reality, the Hill radius of a stellar EMRI is only ~ 2 – 3 times larger than its physical radius, so the artificial enlargement of the Hill radius inflates the gas reservoir available, making a stellar EMRI appear more effective at powering QPEs than it would be in a realistic global potential. In the opposite direction, semi-analytical calculations such as ([I. Linial & B. D. Metzger 2023](#)) ignore the Hill radius entirely. In striking contrast, for a $100 M_\odot$ black hole the Hill radius reaches $R_H \sim 10R_\odot$, which is orders of magnitude larger than

the Bondi radius $\sim 0.02 R_\odot$ used by them to estimate the shocked mass. As a result, a substantial reservoir of gas lying between the Bondi and Hill spheres can be gravitationally perturbed, heated, and later ejected, strongly affecting both the total energy budget and the symmetry of the two-sided flares.

To summarize, only global three-dimensional hydrodynamic simulations that self-consistently include the full gravitational field of the SMBH, which have not been reported in the literature in this context, can properly resolve the relative contribution of the Bondi and Hill reservoirs, quantify the true shocked-gas mass and energy budget, and determine whether stellar-mass black holes can in fact produce the observed QPE properties.

This paper is organized as follows. In [Section 2](#), we analyze the theoretical framework of the EMRI+disk model and estimate relevant timescales and energy budgets. In [Section 3](#), we then describe the setup of our global numerical simulations. Results of star-disk and black holedisk collisions are presented in [Section 4](#). In [Section 5](#), we offer a detailed discussion and further analysis of the EMRI+disk collision model.

2. A QUICK RECAP OF EMRI+DISK MODELS

The EMRI+disk model has gained increasing support from both observational evidence and theoretical analysis. In this model, the energy budget of eruptions comes from EMRI-disk collisions, and two eruptions are produced as the EMRI crosses the disk twice per orbital period. The orbital eccentricity naturally gives rise to alternating short-long intervals and strong – weak outbursts. The Schwarzschild (and Lense–Thirring) precessions of the EMRI orbit cause the intersection point between the orbit and the disk to vary, leading to a changing impact phase from one orbit to the next ([L. J. Dai et al. 2010](#); [J. Xian et al. 2021](#); [C. Zhou et al. 2025](#)). These relativistic precession effects lead to a modulation between two outburst intervals, T_{short} and T_{long} , while keeping the sum $T_{\text{short}} + T_{\text{long}}$ approximately a constant ([C. Zhou et al. 2024a, 2025](#)). This behavior is broadly consistent with observations of GSN 069 and several other QPE sources. Therefore, the EMRI+disk model not only offers a compelling explanation for the energy budget and burst characteristics, but also provides a clear and readily testable theoretical framework for the origin of QPEs. Now it is still unclear whether the secondary object is a star ([I. Linial & B. D. Metzger 2023](#); [I. Linial et al. 2025](#); [I. Linial & B. D. Metzger 2024](#)) or a stellar mass black hole (sBH) ([A. Franchini et al. 2023](#)). Both aim to explain the triggering mechanism, the energy budget, the spectral properties, and the timing structure of QPEs.

In EMRI systems with a sBH as the secondary, passage through the surrounding disk gas can lead to accretion of disk material and the formation of a transient accretion flow, producing radiation powered by accretion. This process can trigger periodic X-ray outbursts, with the luminosity constrained by the Eddington limit

$$L_{\text{Edd}} \approx 1.26 \times 10^{38} \left(\frac{M_{\text{BH}}}{M_{\odot}} \right) \text{ erg/s.} \quad (1)$$

In most QPE events, the observed burst luminosities often exceed 10^{42} erg/s. If this eruption is attributed to Eddington-limited accretion, the required black hole mass must exceed $10^4 M_{\odot}$. On the other hand, if the black hole shocks materials within its Bondi radius $R_{\text{B}} = 2GM_{\text{BH}}/v_{\text{rel}}^2$, a black hole with a mass of $10^4 M_{\odot}$ would still be required to shock a sufficient amount of gas, even with a relatively large impact velocity of $0.1c$ (I. Vurm et al. 2025). However, the rarity of intermediate-mass black holes (IMBHs), with no firm detection yet, renders black hole impacts less favourable than star-disk collisions. However, when applying the star-disk model to the sBH-disk scenario, the effects of the impact inclination and the disk motion are somewhat neglected (A. Franchini et al. 2023).

Here, we highlight the significant impact of the inclination angle i and the disk motion on the relative velocity between the impactor and the disk, thereby strongly influencing various physical parameters such as the energy budget. For a Keplerian disk, the relative velocity can be written as

$$v_{\text{rel}} = 2v_{\text{k}} \sin\left(\frac{i}{2}\right), \quad (2)$$

with v_{k} being the Keplerian velocity. The relative velocity is $v_{\text{k}} \sin i$ if the disk is taken as static, which underestimates the true relative velocity, especially at high inclinations. Moreover, the path length traversed by the impactor within the disk is:

$$\Delta L = 2H / \cos(i/2), \quad (3)$$

where H is the vertical scale height of the disk.

In the stellar EMRI+disk model, a star periodically crosses a TDE disk around a SMBH (I. Linial & B. D. Metzger 2023), with nearly vertical and circular orbits commonly adopted for illustrative purposes and energy estimates. During each disk crossing, the star drives shocks that locally heat the gas, which then expands adiabatically and may emit soft X-rays as blackbody radiation. The mass of shocked gas per collision is expressed as (I. Linial & B. D. Metzger 2023),

$$M_{\text{sh}} = \pi R_{\text{eff}}^2 \Sigma / \cos(i/2), \quad (4)$$

where Σ denotes the local surface density of the accretion disk, and the effective radius R_{eff} is the actual radius over which the disk gas is shocked, usually corresponding to the stellar radius R_{\star} in the star-disk model and to the Bondi radius R_{B} in the sBH-disk model. The factor of $1/\cos(i/2)$ is included because the simplified 2D disk model applies only to collisions perpendicular to a stationary disk, whereas in our case the path length traversed by the impactor varies with the orbital inclination. Assuming the shocked gas is accelerated to the same velocity as the impactor, and for convenience fixing the orbital inclination at $i = \pi/10$, the energy budget of a QPE burst can be approximated by

$$\begin{aligned} E_{\text{sh}} &= \frac{1}{2} M_{\text{sh}} v_{\text{rel}}^2 \\ &\approx 4.3 \times 10^{45} \text{ ergs} \left(\frac{\Sigma}{10^6 \text{ g cm}^{-2}} \right) \left(\frac{R_{\text{eff}}}{R_{\odot}} \right)^2 \left(\frac{v_{\text{rel}}}{0.025c} \right)^2. \end{aligned} \quad (5)$$

Here R_{eff} denotes the effective interaction radius introduced above. In the star-disk model, $R_{\text{eff}} = R_{\star}$ is independent of the relative velocity, leading to $E_{\text{sh,st}} \propto v_{\text{rel}}^2$. In contrast, in the sBH-disk model, the Bondi radius scales as $R_{\text{B}} \propto v_{\text{rel}}^{-2}$, which results in $E_{\text{sh,bh}} \propto v_{\text{rel}}^{-2}$.

To estimate the energy budget in the sBH EMRI+disk model, we adopt a fiducial surface density of 10^6 g cm^{-2} and a sBH of $100 M_{\odot}$ black hole. We assume a SMBH of $M_{\bullet} = 10^6 M_{\odot}$ and an orbital period $T_{\text{orb}} = 63.7 \text{ ks}$, roughly consistent with GSN 069 (G. Miniutti et al. 2019). For an inclination of $i = \pi/10$, the Bondi radius is $R_{\text{B}} \approx 0.68 R_{\odot}$. For comparison, we also show the energy budget assuming an effective interaction radius of $2R_{\text{B}}$, reflecting the possibility that the actual shocked region extends beyond the nominal Bondi radius (see Fig. 2, upper panel).

The energy input can also be reliably estimated from the gravitational drag force acting on the sBH, F_{drag} , and the distance it travels through the disk. This approach is more accurate than the simple approximation $M_{\text{sh}} v_{\text{rel}}^2$, because M_{sh} accounts only for the gas that could be accreted, representing just a fraction of the gas assumed to be shocked across the Bondi radius, whose actual extent typically exceeds the accretion radius by several times. Following C. Zhou et al. (2024a), the sBH energy loss can then be expressed as:

$$\begin{aligned} E_{\text{sBH}} &= F_{\text{drag}} \cdot \Delta L \\ &= 4\pi \ln \Lambda \frac{G^2 m_{\text{sBH}}^2}{v_{\text{rel}}^2} \frac{\Sigma}{\cos(i/2)} \\ &\approx 4 \times 10^{46} \text{ ergs} \left(\frac{\Sigma}{10^6 \text{ g cm}^{-2}} \right) \\ &\quad \left(\frac{m_{\text{sBH}}}{100 M_{\odot}} \right)^2 \left(\frac{\ln \Lambda}{5} \right) \left(\frac{0.024}{\theta(i)} \right), \end{aligned} \quad (6)$$

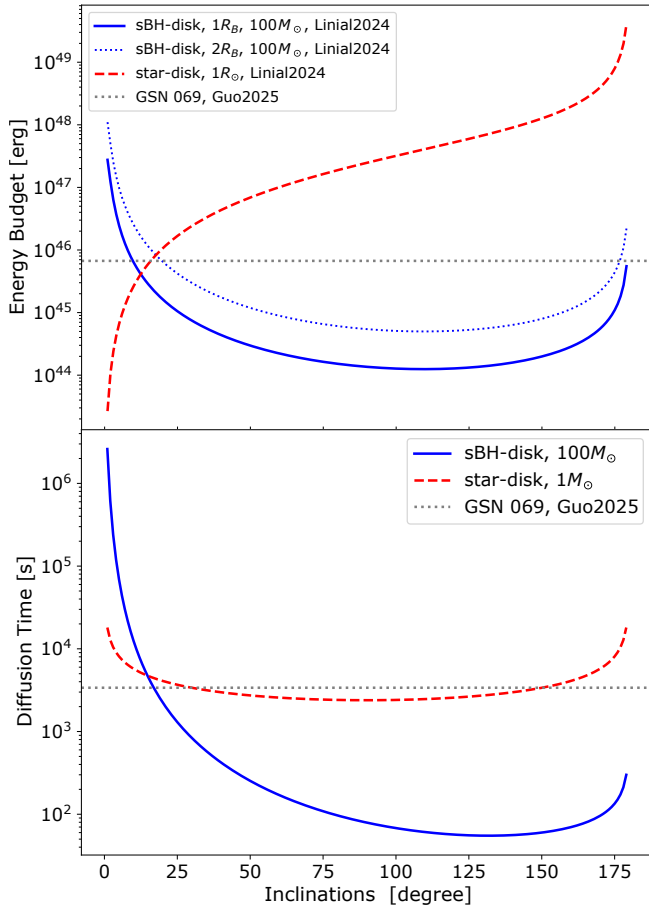


Figure 2. Upper panel: Energy budget estimated with the Linal’s model for a surface density of 10^6 g cm^{-2} . The blue solid and red dashed curves correspond to shocked regions of radius R_B and $2R_B$. The gray dotted line indicates the minimum energy budget observed for GSN 069, $\simeq 7 \times 10^{45} \text{ erg}$ (G. Miniutti et al. 2023; W. Guo & R.-F. Shen 2026). Lower panel: Duration time as a function of inclination. The blue curve shows the prediction of the sBH-disk model, while the red dashed curve corresponds to the star-disk model.

where $\ln \Lambda$ is the Coulomb logarithm, which depends on the ratio of maximum to minimum impact parameters (D. Thun et al. 2016). Here $\theta(i) = \sin^2(i/2) \cos(i/2)$ encapsulates the inclination dependence of the relative velocity and the disk-crossing path length. At low inclinations, the reduced collision velocity enlarges the effective interaction radius, allowing the sBH to shock a substantial portion of the disk gas and produce QPEs. This mechanism also provides a plausible explanation for QPEs powered by sBH without invoking super-Eddington accretion (A. Tsz-Lok Lam et al. 2025), with the effective radius set by the Bondi radius but potentially extending up to the Hill radius.

In addition to the energy budget, the burst duration of QPEs is also of interest and imposes an informative

constraint on QPE models. The eruption duration is set when the photon diffusion timescale becomes comparable to the expansion timescale (I. Linal & B. D. Metzger 2023; I. Vurm et al. 2025),

$$t_e = \left(\frac{\kappa M_{\text{sh}}}{4\pi c v_{\text{rel}}} \right)^{1/2} \approx 4.3 \text{ ks} \left(\frac{\Sigma}{10^6 \text{ g cm}^{-2}} \right)^{1/2} \left(\frac{R_{\text{eff}}}{R_{\odot}} \right) \left(\frac{v_{\text{rel}}}{0.025c} \right)^{-1/2} \left(\frac{\kappa}{0.34 \text{ cm}^2 \text{ g}^{-1}} \right)^{1/2}, \quad (7)$$

where κ is the gas opacity.

Assuming the post-impact debris cloud expands approximately spherically, its optical depth rapidly decreases with time. In the sBH-disk collision model, the duration time is highly sensitive to the orbital inclination (see Fig. 2, lower panel), which exhibits a dependence similar to that of energy budget. This strong sensitivity arises because the effective interaction radius is set by the Bondi radius, which depends on the relative velocity and hence on inclination, leading to the inclination scalings summarized below:

$$t_{e, \text{bh}} \propto \sin^{-5/2}(i/2) \cos^{-1/2}(i/2). \quad (8)$$

For a surface density of 10^6 g cm^{-2} , the duration at an inclination of $\pi/10$ is about 3 ks, which is close to the observed properties of GSN 069. By contrast, in the star-disk model the effective interaction radius is fixed by the stellar radius and is independent of the relative velocity, leading to a much weaker inclination dependence, and hence durations confined to a narrower range of $\sim 3\text{--}13 \text{ ks}$. This inclination scaling can be written as:

$$t_{e, \text{st}} \propto \sin^{-1}(i). \quad (9)$$

The strong inclination sensitivity of the sBH-disk case, spanning nearly three orders of magnitude at low inclinations, may therefore provide a natural explanation for the large diversity of observed QPE durations, although alternative mechanisms may also account for the observed diversity.

In the star-disk model, the burst energy arises primarily from shock compression of the disk gas upon impact, whereas in the sBH-disk interaction, gravitational effects dominate the energy transfer. Numerical simulations have demonstrated that as a black hole traverses the disk, it perturbs the surrounding medium through gravitational drag within its Bondi-Hoyle radius (P. B. Ivanov et al. 1998). The black hole thereby injects part of its orbital kinetic and gravitational potential energy into the disk material, leading to localized heating and substantial radiation output, with our derivation indicating that this mechanism is velocity- and inclination-sensitive. Given that the Eddington luminosity of a

stellar-mass black hole is far below the typical luminosities observed in QPEs, accretion-powered emission can be safely neglected in this scenario.

In the following section, we employ global hydrodynamic simulations to investigate both the star-disk and sBH-disk collision models, allowing us to compare their model predictions.

3. SIMULATION SETUP

In this study, we perform global three-dimensional hydrodynamical simulations of star-disk and sBH-disk collisions using the meshless finite-mass (MFM) method implemented in the GIZMO code (P. F. Hopkins 2015). By computing inter-particle fluxes via Riemann solvers, it can accurately resolve shocks generated during collisions, while also delivering higher computational efficiency compared to alternative SPH methods (P. F. Hopkins 2015). The MFM method maintains second-order consistency in smooth flows, ensuring fast and reliable convergence for both shock capturing and smooth-field evolution (H. Deng et al. 2019). The particle-based method readily allows for global simulations that naturally treat all the gravitational interactions among the SMBH, disk, and star, including their self-gravity (M. Zhang et al. 2025).

We assume a polytropic equation of state with $\gamma = 4/3$ for the gas disk around an SMBH, appropriate for radiation-pressure-dominated gas. Radiative transfer is not included in current simulations. As shown in Fig. 3, the impact affects only a limited portion of the disk that is strictly confined within the Hill radius of the secondary. We can therefore safely restrict the computational domain to a sufficiently large annular sector (the region enclosed by the white solid line in Fig. 3), whose radial and azimuthal extent fully covers a circular area comparable in size to the secondary’s Hill radius. The reduced domain allows us to maintain high resolution around the interaction while preserving the full gravitational potential of the central SMBH, which is essential for accurately capturing the gas dynamics across the Bondi-to-Hill scales. The vertical scale height is fixed to $1 R_\odot$ for both numerical convenience and structural stability, corresponding to a relatively compact disk geometry. The portion of a disk is resolved by $\sim 5 \times 10^6$ particles. We conduct stability tests to ensure that, compared with the initially prescribed disk configuration, no perturbations large enough to affect the subsequent collision simulations are produced. In the relaxation run without collisions, the disk retains a sharp edge and stable structure after 2 hours—twice the duration of the collision simulations—demonstrating its stability.

For the stellar case, we model a self-gravitating polytropic star with solar mass and radius following the Lane-Emden solution with an index corresponding to $\gamma = 5/3$, represented by $\sim 10^5$ particles (see the upper right corner of Fig. 3). This resolution is sufficient to capture the essential interactions with the surrounding disk particles, given that our primary focus is on the gas dynamics and the propagation of perturbations rather than the detailed stellar interior. The stellar-mass black hole, in contrast, is treated as a point mass, since its accretion contributes negligibly to the overall energy budget, the accretion process is neglected.

We focus on the evolution of the accretion disk following the impact by two types of secondary objects—a $100 M_\odot$ black hole and a $1 M_\odot$ star—traversing the disk with orbital parameters that are broadly consistent with GSN 069. Since radiative cooling is not included in our simulations, the post-shock gas retains its thermal energy for an extended period, potentially leading to more pronounced expansion in the later stages than would occur in a realistic cooling environment. The simulations cover a range of disk surface densities (10^4 – 10^6 g cm^{-2}) and different inclination angles ($\pi/10$ and $\pi/2$). Each collision is followed for approximately one hour of simulated time (typical QPE duration of GSN 069), capturing the disk’s immediate reaction to the perturbers, including the propagation of perturbations and the resulting changes in flow structure and density distribution.

4. RESULTS

In this section, we examine how the passage of secondary objects—either a solar-mass star or a stellar-mass black hole—through an accretion disk affects the disk gas. Hydrodynamic simulations provide a controlled setting to systematically explore the influence of different orbital parameters and disk properties on the resulting gas dynamics. Particular attention is given to the morphology, mass, and velocity distribution of the ejecta, as well as the formation of bow shocks and the resulting flow structures. We estimate key parameters, such as the energy budget, to evaluate whether these processes can reproduce the observed features of QPEs.

4.1. Star-Disk collision

From the simulations, we measured the ejecta mass and roughly estimated the energy, which are listed in Table 1 for comparison with theoretical predictions. Here we focus on sBH-disk collision while we performed one star-disk collision simulation (*st_i18_sigma1e6*) to highlight its difference to sBH-disk collisions. In Fig. 4(a), we visualize the flow density near the impact point, with

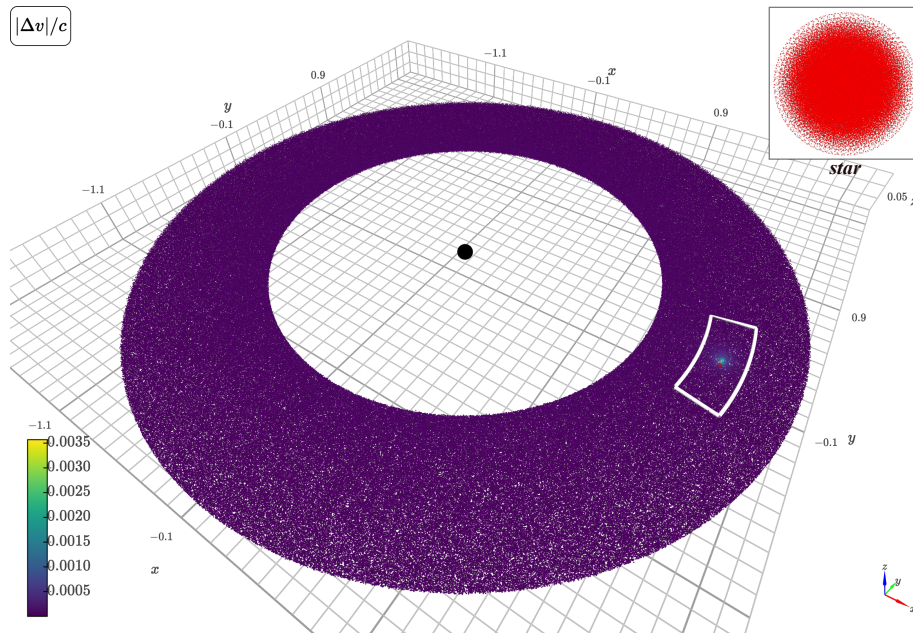


Figure 3. Global simulation of a full accretion disk impacted by an EMRI. The color scale shows the absolute velocity perturbation $|\Delta v|/c$ relative to the unperturbed disk. Regions outside of the Hill sphere remain essentially unaffected by the intruder. The white box outlines the simulation domain we adopted in our production runs. This sector has a radial width of ~ 0.2 AU, and spans an azimuthal angle corresponding to $\sim 1/16$ of the local disk circumference, centered on the impact point. The upper-right panel displays a magnified view of the stellar EMRI resolved by $\sim 10^5$ MFM particles in our simulations.

Table 1. Simulation Results

case	Inclination	Σ (g cm^{-2})	$M_{\text{sh}}^f/M_{\text{sh}}^b$ (M_{\odot}/M_{\odot})	$E_{\text{sh}}^f/E_{\text{sh}}^b$ (erg/erg)	$R_{\text{B}}(\text{or } R_*)/R_{\text{H}}$
<i>bh_i18_sigma1e6</i>	$\pi/10$	10^6	$3.2 \times 10^{-5}/2.9 \times 10^{-5}$	$1.79 \times 10^{46}/1.62 \times 10^{46}$	0.061
<i>bh_i90_sigma1e6</i>	$\pi/2$	10^6	$5.6 \times 10^{-6}/5.2 \times 10^{-6}$	$3.21 \times 10^{44}/2.98 \times 10^{44}$	0.003
<i>bh_i18_sigma1e5</i>	$\pi/10$	10^5	$3.3 \times 10^{-6}/3.4 \times 10^{-6}$	$1.85 \times 10^{45}/1.90 \times 10^{45}$	0.061
<i>bh_i18_sigma1e4</i>	$\pi/10$	10^4	$3.2 \times 10^{-7}/2.8 \times 10^{-7}$	$1.79 \times 10^{44}/1.57 \times 10^{44}$	0.061
<i>st_i18_sigma1e6</i>	$\pi/10$	10^6	$2.0 \times 10^{-5}/3.2 \times 10^{-6}$	$1.12 \times 10^{46}/6.44 \times 10^{44}$	0.421

NOTE— Here “*st/bh*” indicates the impactor type, “*i*” the orbital inclination, and “*sigma*” the disk surface density. The ejecta mass is evaluated at one hour after the impact, and the energy budget is estimated as $\frac{1}{2}M_{\text{sh}}v_{\text{rel}}^2$, where v_{rel} is usually taken to be the relative impact velocity.

arrows indicating the flow velocity. During the impact, a bow shock forms ahead of the star and propagates horizontally, perturbing gas within twice the stellar radius significantly. We define the forward ejecta as moving roughly along the impactor’s trajectory, while the backward ejecta moves oppositely. At the star passage, part of the gas is directly ejected out of the disk, while a low-density wake forms along the star’s trajectory. This region is rapidly refilled with shock-heated gas driven in by strong pressure gradients from both sides, generating backward-directed ejecta.

However, the mass of this backward ejecta is far less than the forward component ($M_{\text{sh}}^f/M_{\text{sh}}^b > 6.3$ in

st_i18_sigma1e6), indicating that the forward outflow dominates both the mass and energy output. This strong asymmetry mainly originates from the physical size of the star, which blocks the downstream flow and produces a rarefied wake region with a density significantly lower than the unperturbed disk. Moreover, the bulk of the forward ejecta moves at nearly the impact velocity with a fast expanding envelope at a speed $\sim 1.8 v_{\text{rel}}$, while the expansion of backward component is slower than $\sim 0.8 v_{\text{rel}}$ (see Fig. 5 (a)). This results in an energy budget differ by over an order of magnitude between the two sides, as estimated from the ejecta kinetic energy. Also, in terms of time evolution, the for-

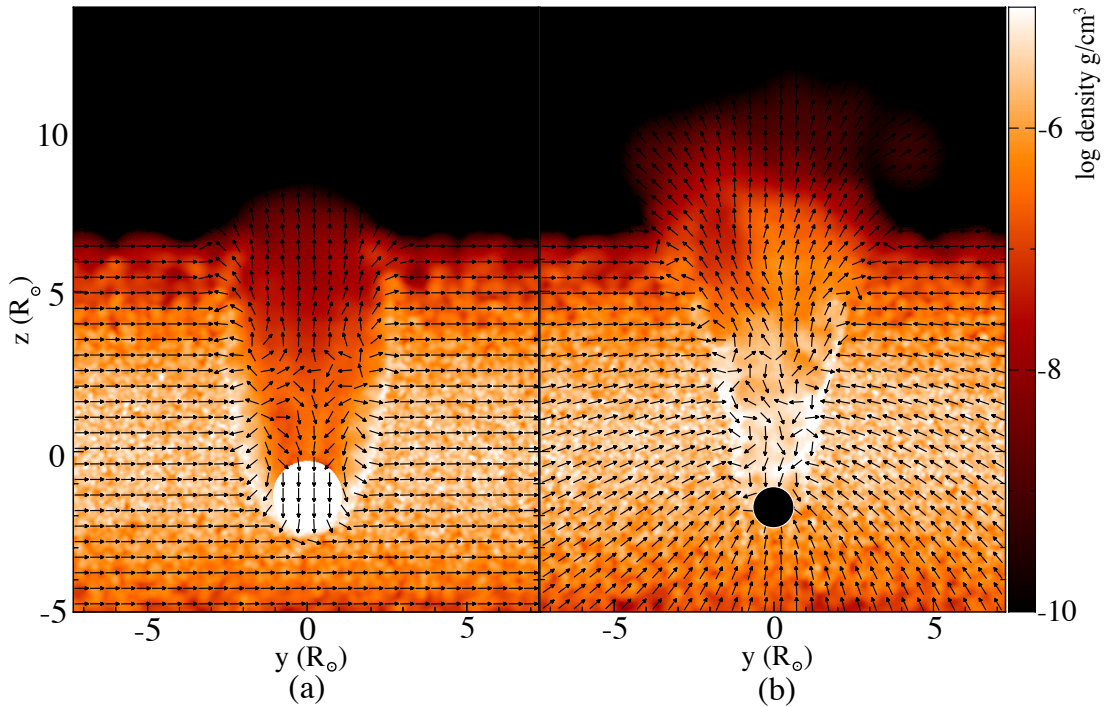


Figure 4. Vertical slices through the disk along the azimuthal direction showing the density distribution and velocity field. Arrow lengths are not to scale. (a) The bow shock is generated by a star-disk collision, and downstream material fills the low-density cavity left by the star’s passage, producing backward ejecta; (b) The perturbation induced by the sBH-disk interaction, exhibiting a bow-shock-like structure. The black hole attracts surrounding material along its path, producing a pronounced density enhancement and quickly generates backward ejecta. (The size of black-filled part is bondi radius of sBH.)

ward ejecta diffuse rapidly and produce sharply peaked energy-release curves, while the backward component contributes more smoothly and over a longer timescale. Consequently, the luminosity becomes increasingly dominated by the forward ejecta, highlighting a forward-backward asymmetry that poses a ‘symmetry problem’ for the star-disk collision model as a viable explanation of QPEs.

Tests with other inclination angles confirm that the strong asymmetry in the ejecta persists. This behavior is consistent with the findings of X. Huang et al. (2025). The authors argue that the strong asymmetry between forward and backward ejecta is most pronounced in the bolometric light curves and in lower-energy bands such as UV and optical, while this asymmetry may be reduced in the soft X-ray band in which QPEs are detected, because the optical depth at soft X-ray frequencies is much lower than the frequency-integrated optical depth used for bolometric calculations.

A crucial difference from previous local simulations (P. Z. Yao et al. 2025; X. Huang et al. 2025) is that our global setup includes the full gravitational potential of the central SMBH. The Hill sphere of the stellar EMRI is restricted to only $\sim 2\text{--}3$ times larger than the stellar radius, which is comparable in size to the bow-shock region. As a result, gravitational perturbations

are highly localized, and the disk material remains essentially undisturbed Keplerian motion outside the bow-shock region (one can compare our Fig. 4(a) with Fig. 10 in P. Z. Yao et al. (2025) and Fig. 2 in X. Huang et al. (2025)).

Finally, our primary focus is the response of the disk gas to the impact under realistic global conditions. The detailed post-impact evolution of the stellar structure itself is not the main subject of this work, as the stellar resolution ($\sim 10^5$ particles) is insufficient to capture subtle internal changes; this will be explored in future studies.

4.2. sBH-Disk collision

In Fig. 4, we show that the interaction of a $100 M_\odot$ black hole with the accretion disk differs from the star-disk case in two fundamental ways. First, the black hole has a negligible physical cross-section and therefore does not obstruct the downstream flow, allowing the wake region to retain a density comparable to or higher than the unperturbed disk. Second, a $100 M_\odot$ black hole possesses a much larger Hill radius ($\sim 10 R_\odot$) than a solar-mass star, enabling it to gravitationally capture and perturb a much greater volume of disk gas. Together, these effects produce significantly larger and far more symmetric ejecta masses on both sides.

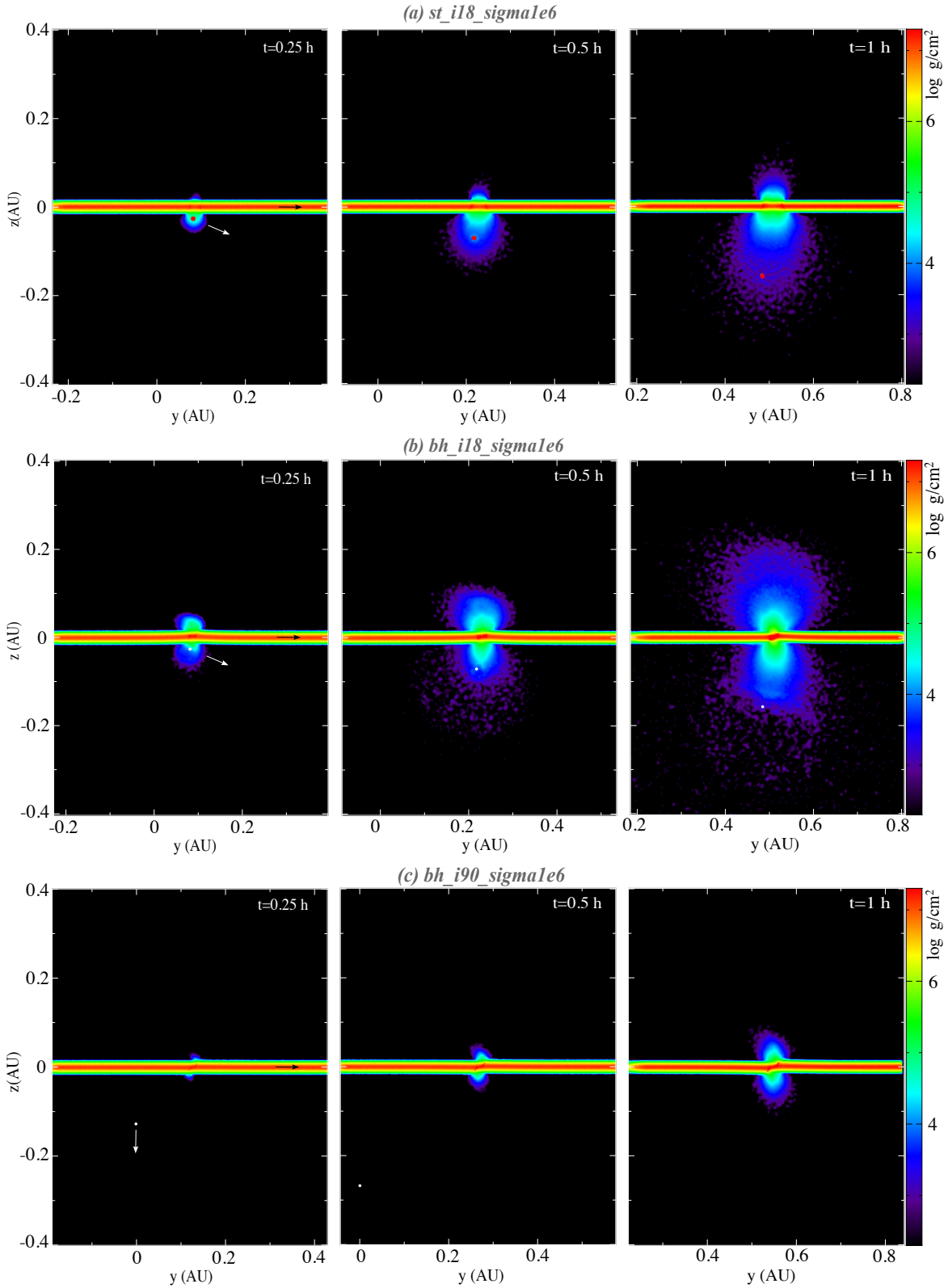


Figure 5. Projected density plot for three simulations in Table 1, which involve stellar or black hole impacts on the disk at inclinations of $\pi/10$ and $\pi/2$. In the first column, arrows mark the directions of motion of both the disk gas and the impactor. For each simulation, the snapshots are shown at 0.25, 0.5, and 1.0 hours after the initial contact.

This improved symmetry is clearly visible in the low-inclination run *bh_i18_sigma1e6* (Fig. 2 (b)): the bulk

of the ejecta moves at roughly the impact velocity, while

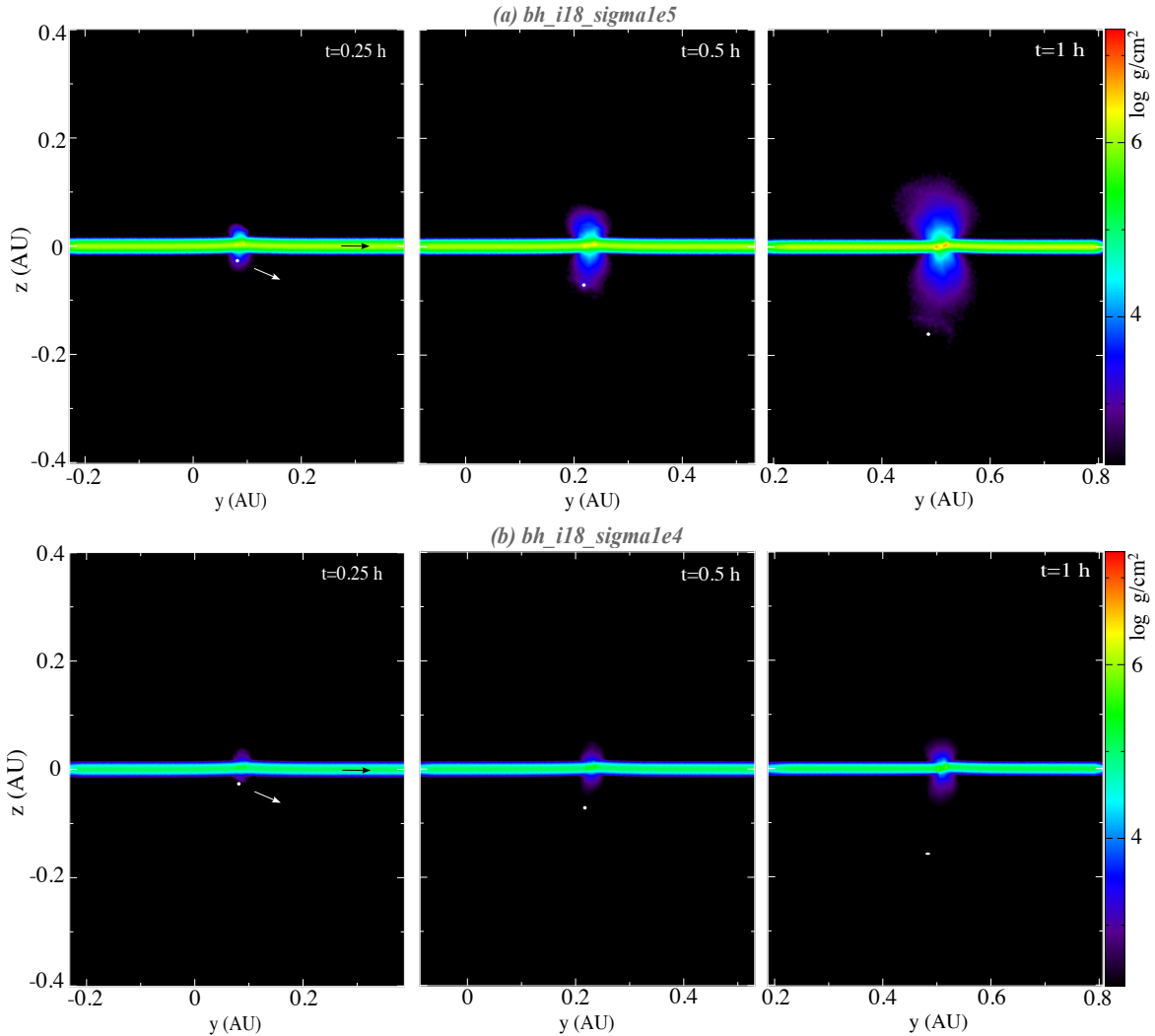


Figure 6. Density projection snapshots for simulations with reduced disk surface densities, compared with the reference case *bh_i18_sigma1e6*. These runs investigate black hole impacts on accretion disks with lower surface densities of 10^5 and 10^4 g cm^{-2} , while all other parameters are kept identical to those in the reference simulation.

the outer layers reach $\sim 2.4 v_{\text{rel}}$ forward and $\sim 1.7 v_{\text{rel}}$ backward, a far milder velocity contrast than in the stellar run *st_i18_sigma1e6* (Fig. 2 (a)), where the forward ejecta expands nearly twice as fast as the backward component. Moreover, the fast-moving outer envelope accounts for only $\sim 10\%$ of the total ejecta mass, so the bulk of the two-sided outflow is only mildly asymmetric, a feature that naturally reproduces the strong-weak flare alternation observed in many QPEs.

The angle of inclination plays an equally decisive role. At low inclination ($i = \pi/10$), the relative velocity drops to $\sim 0.025c$ and the Bondi radius increases to $\sim 2.02 R_{\odot}$ ($\approx 0.18 R_{\text{H}}$). This allows shocked gas to remain longer within the Hill sphere, gaining additional gravitational potential energy before converging on the impact point and thereby substantially boosting the energy budget. In contrast, at high inclination ($i = \pi/2$), the relative

velocity rises to $\sim 0.113c$ and the Bondi radius shrinks to only $\sim 0.66 R_{\odot}$ ($\approx 0.06 R_{\text{H}}$), resulting in a much smaller shocked-gas reservoir and ejecta energy that is insufficient to power bright QPEs such as GSN 069. Runs with lower disk surface densities (*bh_i18_sigma1e5* and *bh_i18_sigma1e4*; also see Fig. 6) further show that the energy budget can be tuned by inclination: lowering the surface density reduces the energy, but this can be compensated by adopting an even smaller inclination angle.

In all simulations, the measured ejecta mass exceeds the analytic predictions based only on the Bondi radius (see Section 2). At low inclination, we infer an effective interaction radius of $\sim 2\text{--}3 R_{\text{B}}$ ($\approx 0.18\text{--}0.27 R_{\text{H}}$), while at high inclination ($i = \pi/2$) the effective radius becomes dramatically larger ($\sim 20 R_{\text{B}} \approx 0.06 R_{\text{H}}$), confirming that the true scale of the interaction is not determined solely by the Bondi radius; the Hill radius

plays a crucial and often dominant role. This strong inclination dependence resolves a long-standing objection: earlier analytic studies (I. Linial & B. D. Metzger 2023) argued that stellar-mass black holes cannot supply enough energy because of their small Bondi radii, requiring IMBHs of $\sim 10^4 M_\odot$. Our simulations show that modest changes in inclination strongly modulate both the relative velocity and the effective interaction radius, making the stellar-mass black-hole scenario fully viable. Moreover, the slower collision speed at low inclination delays the transition from optically thick to optically thin conditions, prolonging the radiative timescale and helping to explain the longer-duration QPEs.

5. DISCUSSION

In this section, we discuss the applicability and limitations of the star-disk and sBH-disk models in light of our simulation results and observational constraints, some of which have already been mentioned in Sections 4. We also outline potential directions for future observational and theoretical investigations.

5.1. Difficulties of Star-Disk Model

Our simulations confirm that star-disk collisions tend to produce strongly asymmetric eruptions. However, the observed strong – weak pattern does not involve such a large contrast; in RX J1301.9+2747, for example, the stronger flare exceeds the weaker one by only a factor of ~ 2 –3. This behavior can be explained more naturally in a sBH-disk system, where orbital eccentricity and impact orientation play key roles. In particular, the highly eccentric orbit of RX J1301.9+2747 likely results in varying impact angles and local disk conditions between successive encounters, producing more noticeable contrasts than in other QPEs. The debris-disk model (P. Z. Yao et al. 2025; I. Linial et al. 2025) may partially explain the backward ejecta, but dedicated numerical simulations are required to verify its feasibility. Future work will focus on these special cases to further clarify their physical origin.

Our simulations suggest that the backward ejecta produce eruptions that are fainter by more than an order of magnitude than the forward component and are therefore likely unobservable. Consequently, if only the forward flare were detected, implying that the observed QPE recurrence time is effectively equal to the stellar orbital period. Under this assumption, additional physical mechanisms are required to explain the commonly observed alternating strong-weak amplitude pattern and the characteristic long-short recurrence intervals.

Adopting the observed QPE recurrence time as the stellar orbital period introduces yet another major dif-

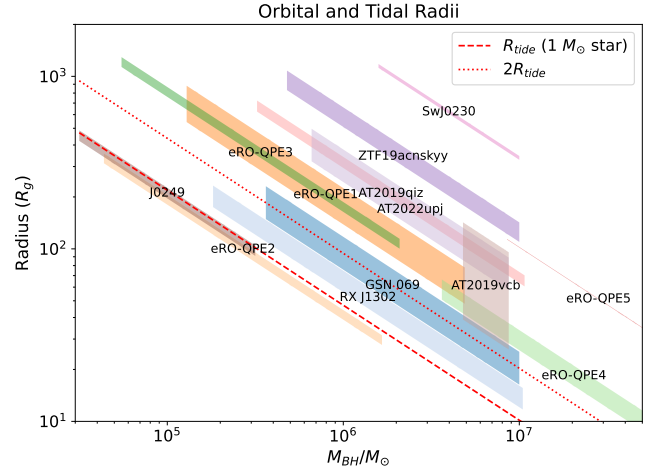


Figure 7. Figure showing the relationship between the circular orbital radius and the tidal radius for a $1 M_\odot$ star as the impactor. According to the simulation results, in most cases only the brighter of the two eruptions is observable, so the observed QPE period effectively corresponds to the star’s orbital period ($T_{\text{orb}} = T_{\text{QPE}}$).

ficulty for the star-disk model. A solar-mass main-sequence star is expected to be fully disrupted if its orbit lies within roughly twice the tidal disruption radius (see e.g., J. Guillochon et al. 2011; S-F. Liu et al. 2013). Comparing the inferred orbital semi-major axes of known QPE sources with this limit (Fig. 7) reveals that most are safely outside the danger zone, but eRO-QPE2, XMMSL J024916.6041244, and RX J1301.9+2747 all lie within $2R_{\text{tide}}$, while GSN 069 sits very close to the threshold. Even under the conservative assumption of a circular orbit with a period twice the observed QPE recurrence time (i.e., neglecting the unobservable backward eruption), two short-period sources remain within twice the tidal radius. This tidal stability problem is therefore severe for a solar-mass star and can only be partially alleviated by adopting a lower-mass impactor.

5.2. Revisiting the Effective Interaction Radius

Our global 3D hydrodynamic simulations demonstrate that simply adopting the Bondi radius as the effective interaction radius $R_{\text{eff}} \sim R_B$, a common assumption in previous analytic work (see Section 2), severely underestimates the true scale of the interaction between a stellar-mass black hole ($\sim 100 M_\odot$) and the accretion disk.

To determine how the effective interaction radius relates to the Bondi and Hill radii, in Fig. 8(a) we first show how the Bondi radius R_B depends on black-hole mass and orbital inclination (since inclination directly controls the relative velocity between the secondary and

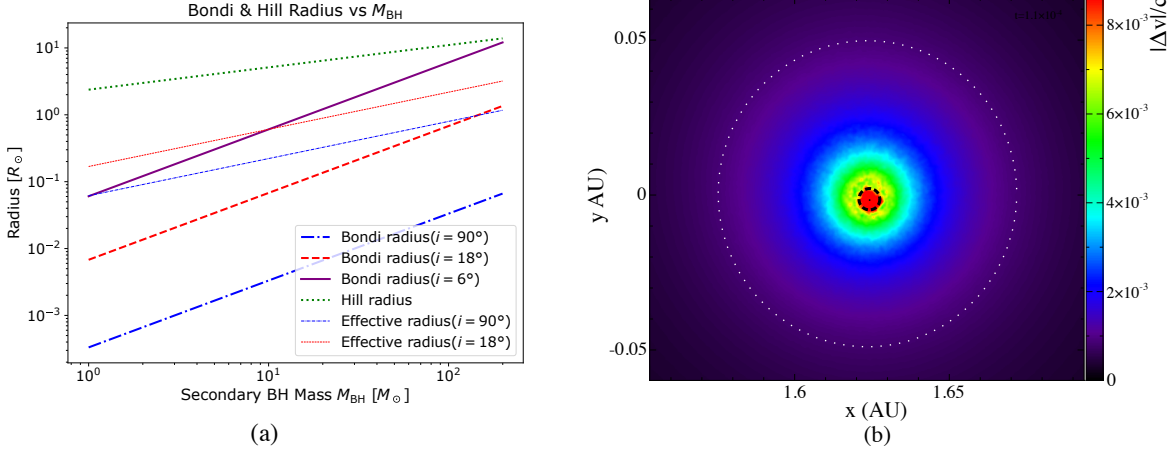


Figure 8. (a) Comparison of Bondi and Hill radii under different impactor masses and orbital inclinations, for a central black hole mass $M_{\text{BH}} = 1.05 \times 10^6 M_{\odot}$ and a semi-major axis $a = 1.62 \text{ AU}$ ($\approx 160 R_g$). Effective radii $i = \pi/10$ and $i = \pi/2$ are shown for reference; (b) Face-on view of the $|\Delta v|$ distribution from the *bh_i18_sigma1e6* simulation at the moment when the black hole passes through the disk mid-plane. The white dotted circle denotes the Hill radius, and the black dashed circle shows the Bondi radius for reference.

the Keplerian disk gas), while the Hill radius R_{H} depends only on mass and orbital separation (both are fixed in our simulations in this work). One can notice that for a $100 M_{\odot}$ black hole, the Hill radius is always larger than the Bondi radius under the physical conditions considered here. And different inclinations can result in variations of Bondi radius by almost two orders of magnitude. Here we mainly discuss low ($i = \pi/10$) and high ($i = \pi/2$) inclinations, and extreme low inclination ($i = \pi/30$) is only for illustration purposes.

In Fig. 8(b), we further illustrate the relative strength of the gravitational pull exerted by the secondary across different radial zones (run *bh_i18_sigma1e6*). The pull is strongest within and near the Bondi radius (black dashed circle) and decays rapidly outward, yet remains dynamically significant throughout the entire Hill sphere (white dotted circle). This qualitative pattern holds at all inclinations, but at lower inclinations the Bondi radius is larger, so the region of strong gravitational influence extends over a correspondingly wider radial range.

In order to quantify the size of the shocked region in a simple and practical way, we propose the following empirical scaling of the effective radius R_{eff} as a replacement for the Bondi radius, which offers a better approximation to the interaction scale than using R_{B} alone:

$$R_{\text{eff}} \simeq 0.5 R_{\text{B}}^{1/3} R_{\text{H}}^{2/3}. \quad (10)$$

This ad hoc relation is not rigorously derived from the simulations but serves as a guess that balances contribution from the Bondi and Hill radii, reproducing the measured ejecta mass and energy budgets more accurately than the estimation with the Bondi radius (see Subsection 5.3 for details).

This empirical relation shows that the effective radius is primarily controlled by the Hill radius (exponent $2/3$), which was completely ignored in previous analytic work. As a result, earlier theoretical calculations severely underestimated the shocked mass produced by an sBH, as they relied solely on the Bondi radius. However, for a given secondary mass and orbital separation, the Hill radius is essentially fixed, so most of the variation in R_{eff} actually comes from changes in the Bondi radius. Although the exponent in R_{B} is only $1/3$, the Bondi radius itself spans more than two orders of magnitude across the relevant range of inclinations (see Fig. 8 (a)). This large dynamic range means that even the weaker dependence on R_{B} produces a major impact on the magnitude of the effective interaction radius, therefore on the mass and flare energy of the shocked gas.

In Fig. 8(a), we show the effective radius as a function of sBH mass for inclination at $i = \pi/10$ and $i = \pi/2$, respectively. For example, at low inclination ($i = \pi/10$), the effective radius is $R_{\text{eff}} \approx 3.2 R_{\text{B}} \approx 0.20 R_{\text{H}} \approx 2.18 R_{\odot}$. At high inclination ($i = \pi/2$), the ratio $R_{\text{eff}}/R_{\text{B}}$ becomes dramatically larger (≈ 24), but the absolute effective radius is actually smaller $R_{\text{eff}} \approx 24 R_{\text{B}} \approx 0.07 R_{\text{H}} \approx 0.8 R_{\odot}$.

5.3. Semi-Analytical Model of sBH-Disk Collisions

In light of results of our global simulations, we develop a semi-analytical model for the shocked mass and gravitational energy gain during the sBH traversal. The model assumes a thin disk with constant scale height $H = 1 R_{\odot}$ and surface density $\Sigma = 10^6 \text{ g cm}^{-2}$, and a secondary black hole mass $m_{\text{sBH}} = 100 M_{\odot}$. The orbital semi-major axis is derived from the period $T_{\text{orb}} = 63.7$

ks and the central SMBH mass $M_\bullet = 10^6 M_\odot$:

$$a = \left(\frac{GM_\bullet T_{\text{orb}}^2}{4\pi^2} \right)^{1/3} \approx 1.597 \text{ AU}. \quad (11)$$

The Hill radius is then

$$R_{\text{H}} = a \left(\frac{m_{\text{sBH}}}{3M_\bullet} \right)^{1/3} \approx 11.05 R_\odot. \quad (12)$$

The relative velocity between the sBH and the disk gas is

$$v_{\text{rel}} = 2v_{\text{k}} \sin\left(\frac{i}{2}\right), \quad (13)$$

where $v_{\text{k}}/c = 0.08$ is the Keplerian speed. The Bondi radius is

$$R_{\text{B}} = \frac{2Gm_{\text{sBH}}}{v_{\text{rel}}^2}. \quad (14)$$

The effective interaction radius follows the empirical scaling in Eq. (10),

$$R_{\text{eff}} = 0.5 R_{\text{B}}^{1/3} R_{\text{H}}^{2/3}. \quad (10)$$

The residence time, i.e. the characteristic timescale over which the sBH traverses the high-density mid-plane of the disk, is defined as

$$\tau \simeq \frac{R_{\text{eff}}}{v_{\text{k}} \sin i}, \quad (15)$$

approximated as the time for a “ball” of size equal to the effective radius R_{eff} to cross the region of peak density. The definition does not depend on the disk scale height H , which is somewhat arbitrary and may vary between sources. Instead, we focus on the mid-plane where the gas density is highest and the gravitational focusing is most efficient. Assuming a Gaussian distribution, the ambient disk density is estimated with the mid-plane density as

$$\rho_0 = \frac{1}{\sqrt{2\pi}} \frac{\Sigma}{H}. \quad (16)$$

The mass accumulation rate, treating the sBH as sweeping a spherical volume, is

$$\dot{M}_{\text{sBH}} = \rho_0 \cdot \frac{4}{3} \pi R_{\text{eff}}^2 v_{\text{rel}}. \quad (17)$$

The shocked mass over the residence time is then

$$M_{\text{sBH}} = \dot{M}_{\text{sBH}} \tau. \quad (18)$$

The energy accumulation rate, reflecting gravitational heating as gas is pulled toward the sBH, is

$$\dot{E}_{\text{sBH}} = \frac{Gm_{\text{sBH}}}{R_\odot^2} \rho_0 v_{\text{rel}} \cdot \frac{4}{3} \pi R_{\text{eff}}^3, \quad (19)$$

where we adopt R_\odot^2 as a characteristic normalization scale to simplify the calculation of order-of-magnitude estimates of the gravitational pull effect. The choice is justified because the key physical length scales involved, such as the Bondi radius R_{B} , the Hill radius R_{H} , and the effective radius R_{eff} derived from simulations, all fall within a range from $\sim 0.03 R_\odot$ to $\sim 10 R_\odot$ depending on the inclination and other parameters. By using a single representative distance R_\odot , we average the gravitational effect over this typical range, avoiding the need for a full integral over radius dependent contributions while still capturing the dominant behavior. Thus, the total gravitational energy gain is

$$E_{\text{sBH}} = \dot{E}_{\text{sBH}} \tau. \quad (20)$$

The expansion speed of the ejecta is estimated as the sound speed in the heated gas, assuming the energy is distributed over the mass:

$$c_s = \sqrt{\frac{E_{\text{sBH}}}{M_{\text{sBH}}}}. \quad (21)$$

For low inclination ($i = 18^\circ$), $v_{\text{rel}} = 0.025c$, $R_{\text{B}} = 0.68 R_\odot$, $R_{\text{eff}} = 2.18 R_\odot$, $\tau = 204.6 \text{ s}$, $\dot{M}_{\text{sBH}} = 2.08 \times 10^{-7} M_\odot \text{ s}^{-1}$, $M_{\text{sBH}} = 4.26 \times 10^{-5} M_\odot$, $\dot{E}_{\text{sBH}} = 1.79 \times 10^{-11} M_\odot R_\odot^2 \text{ s}^{-3}$, $E_{\text{sBH}} = 3.52 \times 10^{46} \text{ erg}$, and $c_s \approx 0.022 c$.

For high inclination ($i = 90^\circ$), $v_{\text{rel}} = 0.113c$, $R_{\text{B}} = 0.033 R_\odot$, $R_{\text{eff}} = 0.80 R_\odot$, $\tau = 23.1 \text{ s}$, $\dot{M}_{\text{sBH}} = 1.26 \times 10^{-7} M_\odot \text{ s}^{-1}$, $M_{\text{sBH}} = 2.91 \times 10^{-6} M_\odot$, $\dot{E}_{\text{sBH}} = 3.96 \times 10^{-12} M_\odot R_\odot^2 \text{ s}^{-3}$, $E_{\text{sBH}} = 8.81 \times 10^{44} \text{ erg}$, and $c_s \approx 0.013 c$.

This simple semi-analytical framework qualitatively reproduces the simulation trend of higher accreted mass (one order of magnitude), faster speed of ejecta (a factor of two) and energy (two orders of magnitude) at low inclinations, driven by larger R_{eff} (from slower v_{rel}) and longer residence time τ . Besides, the R_{eff}^3 scaling in \dot{E}_{sBH} emphasizes volume-like heating, amplifying the energy difference. Modulations induced by these parameters match observed QPE variations, with low inclinations causing strong flares and high inclinations leading to weaker events, explaining alternating patterns and diversity in recurrence and luminosities.

5.4. Implications

Based on our semi-analytical model, fitting the energy budget of GSN 069 does not necessarily require a secondary as massive as $100 M_\odot$. For a disk surface density of 10^6 g cm^{-2} , an sBH with a mass of $\sim 50 M_\odot$ can already provide sufficient energy at an inclination of $i = \pi/10$, and it is expected that the required mass increases at higher inclinations. Since the burst energy

of different QPEs span $\sim 10^{44}$ – 10^{48} erg, the sBH-disk model can accommodate a variety of cases within this range, providing a viable explanation.

Because the EMRI usually has a mild eccentricity, the two impacts in one orbital period may not necessarily have the same inclination angle. Such a discrepancy may contribute to the strong-weak patterns of outbursts. In this work, however, we fixed the inclination to investigate the origins of ejecta mass and energy source for sBHs impacting disks with a realistic global potential. Effects caused by variations of consecutive impacts are left for future studies.

In addition, we refrain from studying BHs more massive than $\sim 100 M_{\odot}$. For more massive secondary black holes, the larger effective interaction radius and Hill radius during disk crossings lead to stronger perturbations, and repeated passages can progressively disrupt the accretion disk’s structure. Once the disk can no longer maintain its morphology, it becomes unable to support the stable periodicity required in QPE models. Therefore, some QPEs with poorer periodic coherence (e.g., eRO-QPE1) may be the result of interactions involving more massive black holes. In future work, we will further investigate the secular evolution of the system, encompassing both the disk structure and orbital dynamics, under perturbations from a binary BH system. This mechanism may be related to the newly discovered QPE source Ansky (L. Hernández-García et al. 2025a,b)—whose long-term monitoring shows a doubling of the recurrence period, and more generally to sources with irregular recurrence and sources whose recurrence period evolves secularly over time.

Note that numerical simulations of extremely long-period QPEs or very thick accretion disks remain challenging, and our current study does not include radiation transfer. Addressing these aspects, together with multi-wavelength observations and more refined simulations, will be essential to identify sBH-disk collisions and to further improve our understanding of QPE formation mechanisms.

6. SUMMARY

With a series of 3D global mesh-free hydrodynamic simulations, we carefully compare different EMRI+disk models taking into account the potential of the central SMBH, which is normally ignored. The star-disk and sBH-disk collisions exhibit different inclination dependence in both the energy output and the diffusion timescale. This difference arises from the distinct mechanisms of energy generation: in the star-disk model, energy is primarily transferred through direct collision, accelerating the mass within the stellar cross-section,

whereas in the sBH-disk model, energy is imparted via gravitational pull on the disk gas, with the effective interaction radius R_{eff} playing a key role in scaling the shocked mass and energy.

Although sufficient energy can be injected into the disk by stellar collisions, the resulting eruptions are highly asymmetric. In other words, either only one side of eruptions could be observed, or consecutive eruptions exhibit large variations in brightness. Neither of these features are consistent with the observations. In addition, durations of outbursts produced by stellar impacts are in a relatively narrow range, making it difficult to account for the large diversity of QPEs, especially for the ultra-long-duration events. Besides, the sustainability of a main sequence star against tides in an orbit with such short periods around the SMBH is another concern.

In contrast, the sBH-disk model is more attractive. A stellar-mass black hole $m_{\text{sBH}} \sim 50 M_{\odot}$ passing through the accretion disk at a low inclination can produce energetic nearly symmetric two-sided ejecta, sufficient to explain sources like GSN 069. The moderate strong-weak alternation between consecutive flares of QPEs can be attributed to variations between two impacts in one orbital period of the sBH. Our semi-analytical model, calibrated to simulations, confirms that sBH impacts can power the full QPE energy range (10^{44} - 10^{48} erg) without invoking an IMBH as in previous estimates relying solely on the Bondi radius. Incorporating the effective radius dependence $R_{\text{eff}} \simeq 0.5 R_{\text{B}}^{1/3} R_{\text{H}}^{2/3}$ corrects this, showing that the Hill radius dominates the scaling and enables realistic energy generation even for sBHs. Besides, the range of eruption durations is more consistent with the observations. Unlike stellar EMRIs the lifetime of an sBH is not a limiting factor. However, it is necessary to consider the long-term stability of the disk under the perturbation of an sBH. It can be straightforward to demonstrate that the disk remains stable over thousands of passages of an sBH with global N -body simulations (H. Rein & S.-F. Liu 2012) containing the SMBH and sBH treating the disk with test particles.

In summary, we conclude that the dynamics of the sBH-disk model matches observations more closely, providing a reasonable and robust explanation for the origin of QPEs. Future work will further explore the parameter space and incorporate radiative transfer and relativistic corrections. We plan to perform systematic, source-by-source modeling of cataloged QPEs to enable quantitative comparison with observations. High-cadence, multi-wavelength observations, together with gravitational wave detections, will be essential to test the sBH-disk model and constrain parameters of QPE systems. In particular, confirming that the EMRIs responsible for

QPEs are sBHs rather than stars would be highly significant. It would offer a unique opportunity to probe the environment around supermassive black holes, implying that such sBHs may be ubiquitous and positioning them as promising targets for space-based gravitational wave observatories (L. Lui et al. 2025).

ACKNOWLEDGMENTS

We are grateful to Junping Chen, Xian Chen, Wenyuan Guo, Ning Jiang, Shuo Li, Bo Ma, Erlin Qiao, Ruiqi

Yang, and Yong Zhang for valuable exchanges. In addition, we thank the participants of the TDE FORUM (Full-process Orbital to Radiative Unified Modeling) online seminar series for their inspiring discussions.

REFERENCES

- Arcodia, R., Merloni, A., Nandra, K., et al. 2021, *Nature*, 592, 704, doi: [10.1038/s41586-021-03394-6](https://doi.org/10.1038/s41586-021-03394-6)
- Arcodia, R., Liu, Z., Merloni, A., et al. 2024, *A&A*, 684, A64, doi: [10.1051/0004-6361/202348881](https://doi.org/10.1051/0004-6361/202348881)
- Arcodia, R., Baldini, P., Merloni, A., et al. 2025, *ApJ*, 989, 13, doi: [10.3847/1538-4357/adc9b](https://doi.org/10.3847/1538-4357/adc9b)
- Baldini, P., et al. 2026, doi: [10.1051/0004-6361/202558241](https://doi.org/10.1051/0004-6361/202558241)
- Chakraborty, J., Kara, E., Masterson, M., et al. 2021, *ApJL*, 921, L40, doi: [10.3847/2041-8213/ac313b](https://doi.org/10.3847/2041-8213/ac313b)
- Chakraborty, J., Kara, E., Arcodia, R., et al. 2025, *ApJL*, 983, L39, doi: [10.3847/2041-8213/adc2f8](https://doi.org/10.3847/2041-8213/adc2f8)
- Chakraborty, J., et al. 2025, *Astrophys. J. Lett.*, 983, L39, doi: [10.3847/2041-8213/adc2f8](https://doi.org/10.3847/2041-8213/adc2f8)
- Chakraborty, J., et al. 2026, <https://arxiv.org/abs/2602.16776>
- Chashkina, A., Bromberg, O., Levinson, A., & Nakar, E. 2024, *A&A*, 691, A313, doi: [10.1051/0004-6361/202348635](https://doi.org/10.1051/0004-6361/202348635)
- Dai, L. J., Fuerst, S. V., & Blandford, R. 2010, *MNRAS*, 402, 1614, doi: [10.1111/j.1365-2966.2009.16038.x](https://doi.org/10.1111/j.1365-2966.2009.16038.x)
- Deng, H. 2025, arXiv preprint arXiv:2507.09578
- Deng, H., Mayer, L., Latter, H., Hopkins, P. F., & Bai, X.-N. 2019, *The Astrophysical Journal Supplement Series*, 241, 26
- Evans, P. A., Nixon, C. J., Campana, S., et al. 2023, *Nature Astronomy*, 7, 1368, doi: [10.1038/s41550-023-02073-y](https://doi.org/10.1038/s41550-023-02073-y)
- Franchini, A., Bonetti, M., Lupi, A., et al. 2023, *A&A*, 675, A100, doi: [10.1051/0004-6361/202346565](https://doi.org/10.1051/0004-6361/202346565)
- Giustini, M., Miniutti, G., & Saxton, R. D. 2020, *A&A*, 636, L2, doi: [10.1051/0004-6361/202037610](https://doi.org/10.1051/0004-6361/202037610)
- Guillochon, J., Ramirez-Ruiz, E., & Lin, D. 2011, *ApJ*, 732, 74, doi: [10.1088/0004-637X/732/2/74](https://doi.org/10.1088/0004-637X/732/2/74)
- Guo, W., & Shen, R.-F. 2026, *ApJ*, 998, 78, doi: [10.3847/1538-4357/ae3562](https://doi.org/10.3847/1538-4357/ae3562)
- Hernández-García, L., Chakraborty, J., Sánchez-Sáez, P., et al. 2025a, *Nature Astronomy*, 9, 895, doi: [10.1038/s41550-025-02523-9](https://doi.org/10.1038/s41550-025-02523-9)
- Hernández-García, L., Sánchez-Sáez, P., Chakraborty, J., et al. 2025b, arXiv e-prints, arXiv:2509.16304, doi: [10.48550/arXiv.2509.16304](https://doi.org/10.48550/arXiv.2509.16304)
- Hopkins, P. F. 2015, *MNRAS*, 450, 53, doi: [10.1093/mnras/stv195](https://doi.org/10.1093/mnras/stv195)
- Huang, X., Linial, I., & Jiang, Y.-F. 2025, *ApJ*, 993, 186, doi: [10.3847/1538-4357/ae07ca](https://doi.org/10.3847/1538-4357/ae07ca)
- Ivanov, P. B., Igumenshchev, I. V., & Novikov, I. D. 1998, *ApJ*, 507, 131, doi: [10.1086/306324](https://doi.org/10.1086/306324)
- Jiang, N., & Pan, Z. 2025, *Astrophys. J. Lett.*, 983, L18, doi: [10.3847/2041-8213/adc456](https://doi.org/10.3847/2041-8213/adc456)
- Kaur, K., Stone, N. C., & Gilbaum, S. 2023, *MNRAS*, 524, 1269, doi: [10.1093/mnras/stad1894](https://doi.org/10.1093/mnras/stad1894)
- King, A. 2020, *MNRAS*, 493, L120, doi: [10.1093/mnrasl/slaa020](https://doi.org/10.1093/mnrasl/slaa020)
- Krolik, J. H., & Linial, I. 2022, *ApJ*, 941, 24, doi: [10.3847/1538-4357/ac9eb6](https://doi.org/10.3847/1538-4357/ac9eb6)
- Linial, I., & Metzger, B. D. 2023, *ApJ*, 957, 34, doi: [10.3847/1538-4357/acf65b](https://doi.org/10.3847/1538-4357/acf65b)
- Linial, I., & Metzger, B. D. 2024, *ApJL*, 963, L1, doi: [10.3847/2041-8213/ad2464](https://doi.org/10.3847/2041-8213/ad2464)
- Linial, I., Metzger, B. D., & Quataert, E. 2025, arXiv e-prints, arXiv:2506.10096, doi: [10.48550/arXiv.2506.10096](https://doi.org/10.48550/arXiv.2506.10096)
- Liu, S.-F., Guillochon, J., Lin, D. N. C., & Ramirez-Ruiz, E. 2013, *ApJ*, 762, 37, doi: [10.1088/0004-637X/762/1/37](https://doi.org/10.1088/0004-637X/762/1/37)
- Lu, W., & Quataert, E. 2023, *MNRAS*, 524, 6247, doi: [10.1093/mnras/stad2203](https://doi.org/10.1093/mnras/stad2203)
- Lui, L., Torres-Orjuela, A., Chowdhury, R. K., & Dai, L. 2025, arXiv e-prints, arXiv:2508.07961, doi: [10.48550/arXiv.2508.07961](https://doi.org/10.48550/arXiv.2508.07961)
- Metzger, B. D., Stone, N. C., & Gilbaum, S. 2022, *ApJ*, 926, 101, doi: [10.3847/1538-4357/ac3ee1](https://doi.org/10.3847/1538-4357/ac3ee1)

- Miniutti, G., Giustini, M., Arcodia, R., et al. 2023, *A&A*, 670, A93, doi: [10.1051/0004-6361/202244512](https://doi.org/10.1051/0004-6361/202244512)
- Miniutti, G., Saxton, R. D., Giustini, M., et al. 2019, *Nature*, 573, 381, doi: [10.1038/s41586-019-1556-x](https://doi.org/10.1038/s41586-019-1556-x)
- Nicholl, M., Pasham, D. R., Mummery, A., et al. 2024, *Nature*, 634, 804, doi: [10.1038/s41586-024-08023-6](https://doi.org/10.1038/s41586-024-08023-6)
- Pan, X., Li, S.-L., & Cao, X. 2023, *ApJ*, 952, 32, doi: [10.3847/1538-4357/acd180](https://doi.org/10.3847/1538-4357/acd180)
- Pan, X., Li, S.-L., Cao, X., Miniutti, G., & Gu, M. 2022, *ApJL*, 928, L18, doi: [10.3847/2041-8213/ac5faf](https://doi.org/10.3847/2041-8213/ac5faf)
- Pan, Z., & Lai, D. 2026, <https://arxiv.org/abs/2601.22465>
- Pasham, D., Coughlin, E., Nixon, C., et al. 2024, arXiv e-prints, arXiv:2411.05948, doi: [10.48550/arXiv.2411.05948](https://doi.org/10.48550/arXiv.2411.05948)
- Raj, A., & Nixon, C. J. 2021, *ApJ*, 909, 82, doi: [10.3847/1538-4357/abdc25](https://doi.org/10.3847/1538-4357/abdc25)
- Rein, H., & Liu, S.-F. 2012, *A&A*, 537, A128, doi: [10.1051/0004-6361/201118085](https://doi.org/10.1051/0004-6361/201118085)
- Śniegowska, M., Grzędziński, M., Czerny, B., & Janiuk, A. 2023, *A&A*, 672, A19, doi: [10.1051/0004-6361/202243828](https://doi.org/10.1051/0004-6361/202243828)
- Suková, P., Zajaček, M., Witzany, V., & Karas, V. 2021, *ApJ*, 917, 43, doi: [10.3847/1538-4357/ac05c6](https://doi.org/10.3847/1538-4357/ac05c6)
- Sun, L., Shu, X., & Wang, T. 2013, *ApJ*, 768, 167, doi: [10.1088/0004-637X/768/2/167](https://doi.org/10.1088/0004-637X/768/2/167)
- Tagawa, H., & Haiman, Z. 2023, *MNRAS*, 526, 69, doi: [10.1093/mnras/stad2616](https://doi.org/10.1093/mnras/stad2616)
- Thun, D., Kuiper, R., Schmidt, F., & Kley, W. 2016, *A&A*, 589, A10, doi: [10.1051/0004-6361/201527629](https://doi.org/10.1051/0004-6361/201527629)
- Tsz-Lok Lam, A., Shibata, M., Kawaguchi, K., & Pelle, J. 2025, arXiv e-prints, arXiv:2504.17016, doi: [10.48550/arXiv.2504.17016](https://doi.org/10.48550/arXiv.2504.17016)
- Vurm, I., Linial, I., & Metzger, B. D. 2025, *ApJ*, 983, 40, doi: [10.3847/1538-4357/adb74d](https://doi.org/10.3847/1538-4357/adb74d)
- Wang, M., Yin, J., Ma, Y., & Wu, Q. 2022, *ApJ*, 933, 225, doi: [10.3847/1538-4357/ac75e6](https://doi.org/10.3847/1538-4357/ac75e6)
- Wevers, T., & French, K. D. 2024, *ApJL*, 969, L17, doi: [10.3847/2041-8213/ad5725](https://doi.org/10.3847/2041-8213/ad5725)
- Wevers, T., Pasham, D. R., Jalan, P., Rakshit, S., & Arcodia, R. 2022, *A&A*, 659, L2, doi: [10.1051/0004-6361/202243143](https://doi.org/10.1051/0004-6361/202243143)
- Wu, M., Jiang, N., Zhu, J., et al. 2025, *Astrophys. J. Lett.*, 988, L77, doi: [10.3847/2041-8213/adf229](https://doi.org/10.3847/2041-8213/adf229)
- Xian, J., Zhang, F., Dou, L., He, J., & Shu, X. 2021, *ApJL*, 921, L32, doi: [10.3847/2041-8213/ac31aa](https://doi.org/10.3847/2041-8213/ac31aa)
- Xiong, Y., Jiang, N., Pan, Z., Hao, L., & Li, Z. 2025, *Astrophys. J.*, 989, 49, doi: [10.3847/1538-4357/ade2d7](https://doi.org/10.3847/1538-4357/ade2d7)
- Yao, P. Z., Quataert, E., Jiang, Y.-F., Lu, W., & White, C. J. 2025, *ApJ*, 978, 91, doi: [10.3847/1538-4357/ad8911](https://doi.org/10.3847/1538-4357/ad8911)
- Zalamea, I., Menou, K., & Beloborodov, A. M. 2010, *MNRAS*, 409, L25, doi: [10.1111/j.1745-3933.2010.00930.x](https://doi.org/10.1111/j.1745-3933.2010.00930.x)
- Zhang, M., Zhang, W., Deng, H., Guo, H., & Sun, J. 2025, *The Astrophysical Journal*, 993, 244
- Zhao, Z. Y., Wang, Y. Y., Zou, Y. C., Wang, F. Y., & Dai, Z. G. 2022, *A&A*, 661, A55, doi: [10.1051/0004-6361/202142519](https://doi.org/10.1051/0004-6361/202142519)
- Zhou, C., Huang, L., Guo, K., Li, Y.-P., & Pan, Z. 2024a, *PhRvD*, 109, 103031, doi: [10.1103/PhysRevD.109.103031](https://doi.org/10.1103/PhysRevD.109.103031)
- Zhou, C., Pan, Z., Jiang, N., & Zhao, W. 2025, *Mon. Not. Roy. Astron. Soc.*, 543, 1816, doi: [10.1093/mnras/staf1580](https://doi.org/10.1093/mnras/staf1580)
- Zhou, C., Zeng, Y., & Pan, Z. 2025, *ApJ*, 985, 242, doi: [10.3847/1538-4357/adcee2](https://doi.org/10.3847/1538-4357/adcee2)
- Zhou, C., Zhong, B., Zeng, Y., Huang, L., & Pan, Z. 2024b, *PhRvD*, 110, 083019, doi: [10.1103/PhysRevD.110.083019](https://doi.org/10.1103/PhysRevD.110.083019)
- Zhu, J., Jiang, N., Wang, Y., et al. 2025, *ApJL*, 994, L16, doi: [10.3847/2041-8213/ae19ea](https://doi.org/10.3847/2041-8213/ae19ea)